# Supplementary Material for

## Selective $CO_2$ electrolysis to CO using isolated antimony alloyed copper

Jiawei Li†, Hongliang Zeng†, Xue Dong†, Yimin Ding, Sunpei Hu, Runhao Zhang, Yizhou Dai, Peixin Cui, Zhou Xiao, Donghao Zhao, Liujiang Zhou, Tingting Zheng, Jianping Xiao*, Jie Zeng*, Chuan Xia*

*Corresponding authors: xiao@dicp.ac.cn (J.X.); zengj@ustc.edu.cn (J.Z.); chuan.xia@uestc.edu.cn (C.X.)

†These authors contributed equally to this work.

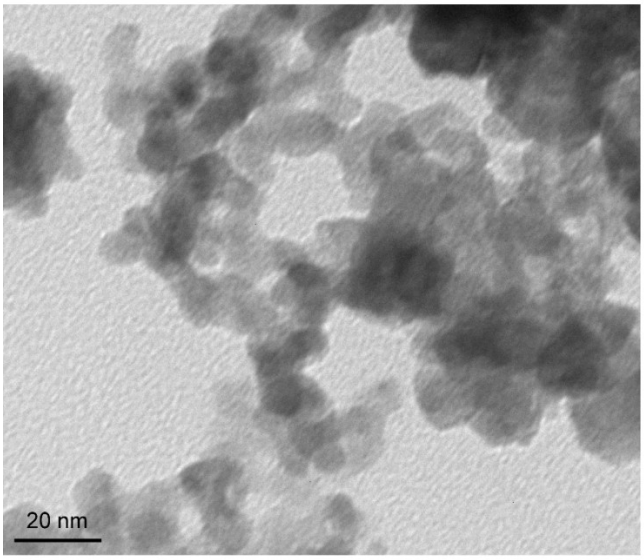


**Supplementary Fig. 1 | TEM image of $Sb_1Cu$-5.** The image showed nanoparticles with a homogeneous morphology and sizes ranging from 10 to 20 nm.

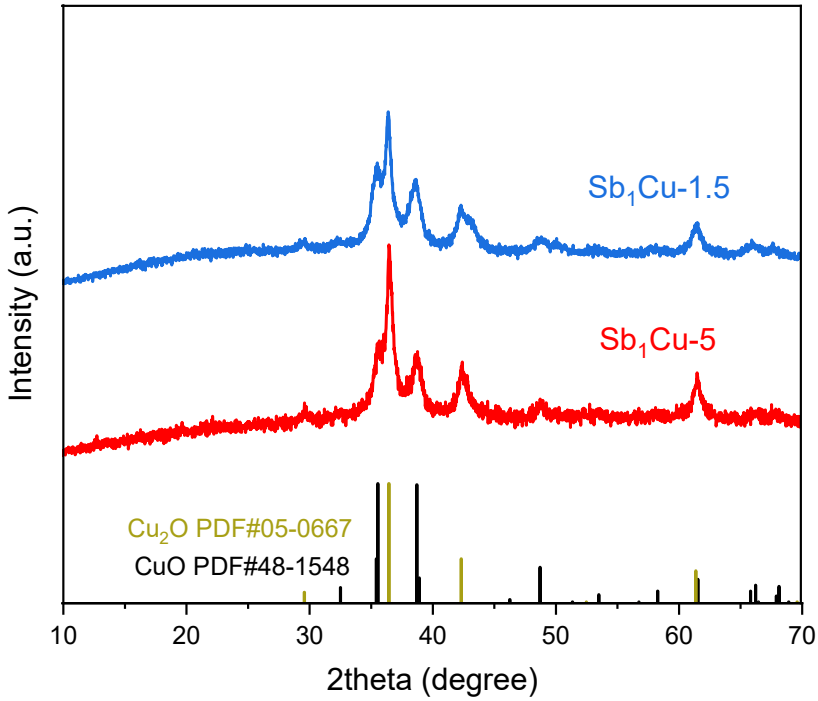


**Supplementary Fig. 2 | PXRD patterns of as-prepared $Sb_1Cu$ catalysts.** The peaks were consistent with standard $Cu_2O$ and CuO. No Sb or Sb oxides diffraction peaks were found, excluding the formation of Sb nanoparticles. The formation of copper oxides was due to the fact that Cu nanocrystal surface is oxygen susceptible when exposed to air.

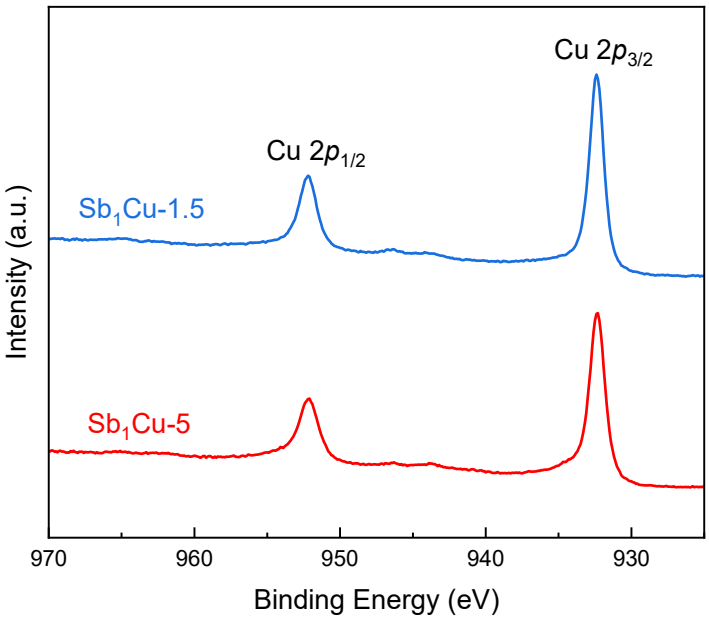


**Supplementary Fig. 3 | Cu 2*p* XPS spectra of as-prepared $Sb_1Cu$ catalysts.** The peaks at 952.2 eV and 932.3 eV were assigned to Cu $2p_{1/2}$ and Cu $2p_{3/2}$, respectively.

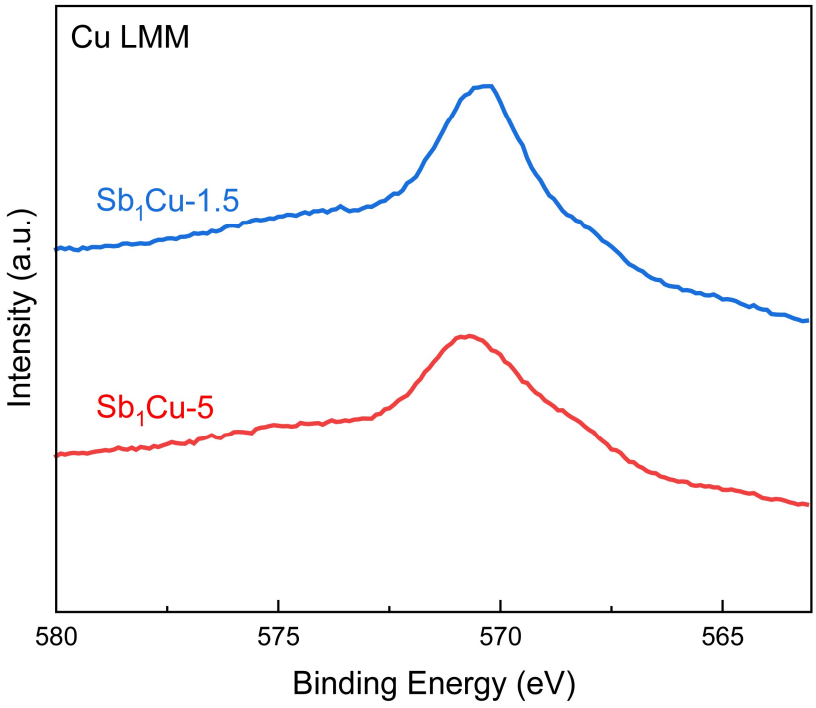


**Supplementary Fig. 4 | Cu LMM Auger XPS spectra of as-prepared $Sb_1Cu$ catalysts.** The peaks at approximately 570 eV were assigned to $Cu^I$, confirming the spontaneous oxidation of the as-prepared $Sb_1Cu$ catalysts.

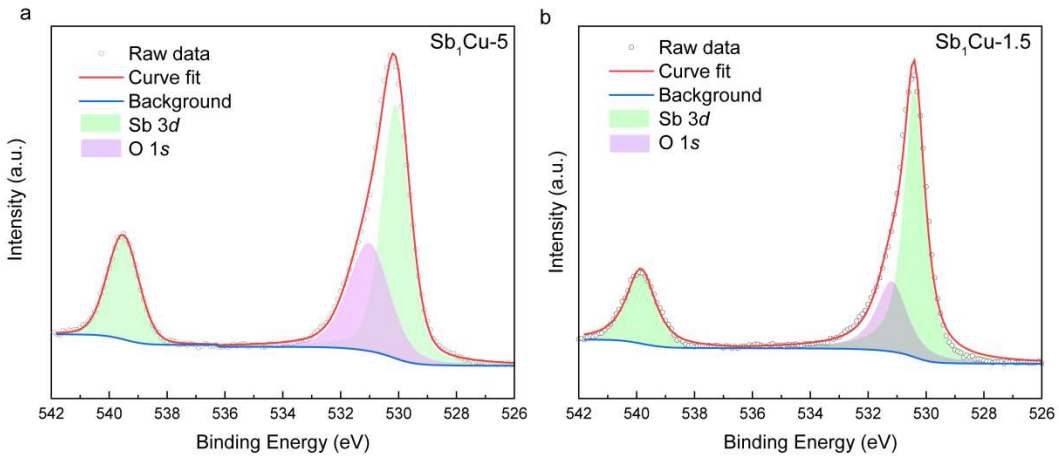


**Supplementary Fig. 5 | Sb 3*d* XPS spectra of as-prepared a) $Sb_1Cu$-5 and b) $Sb_1Cu$-1.5 catalysts.** The peaks at approximately 539.7 eV and 530.3 eV were assigned to Sb $3d_{3/2}$ and Sb $3d_{5/2}$, respectively, confirming the oxidation state of $Sb^{III}$.

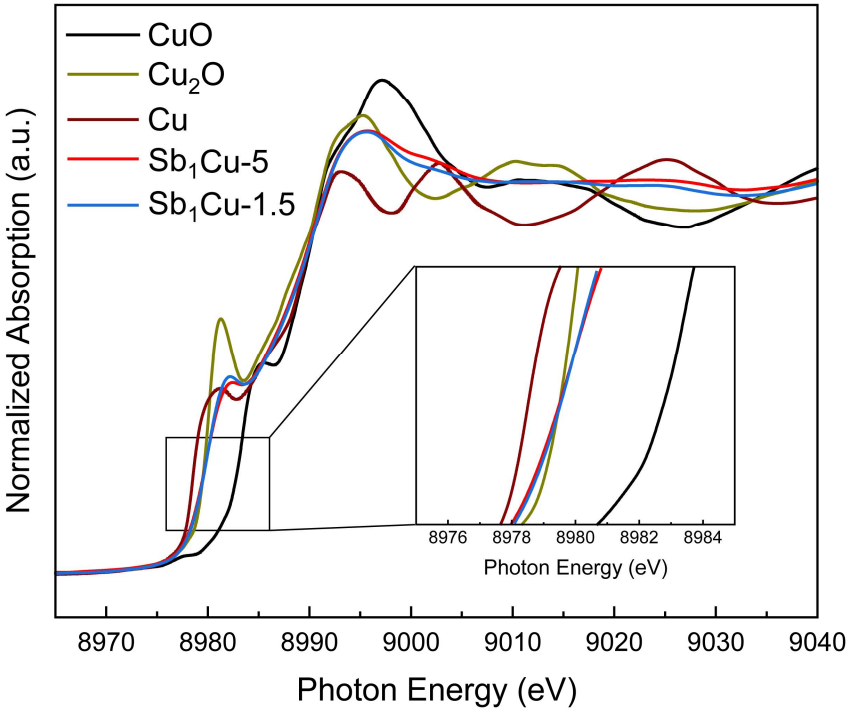


**Supplementary Fig. 6 | Cu *K*-edge XANES spectra of as-prepared $Sb_1Cu$ catalysts.** Cu foil, $Cu_2O$ and CuO were used as references for $Cu^0$, $Cu^I$ and $Cu^{II}$, respectively. The near edge positions of the catalysts were consistent with the $Cu_2O$ standard sample (inset of the figure), confirming the oxidation state of $Cu^I$ in the as-synthesized $Sb_1Cu$ catalysts.

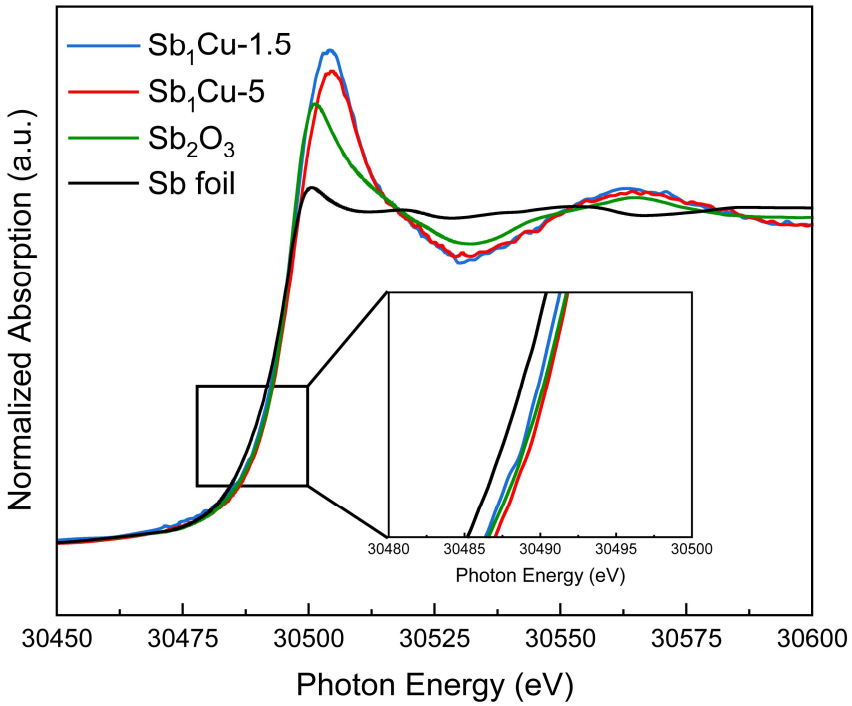


**Supplementary Fig. 7 | Sb *K*-edge XANES spectra of as-prepared $Sb_1Cu$ catalysts.** Sb foil and $Sb_2O_3$ were used as references for $Sb^0$, $Sb^{III}$, respectively. The near edge positions of the catalysts were consistent with the $Sb_2O_3$ standard sample (inset of the figure), confirming the oxidation state of $Sb^{III}$ in the as-synthesized $Sb_1Cu$ samples.

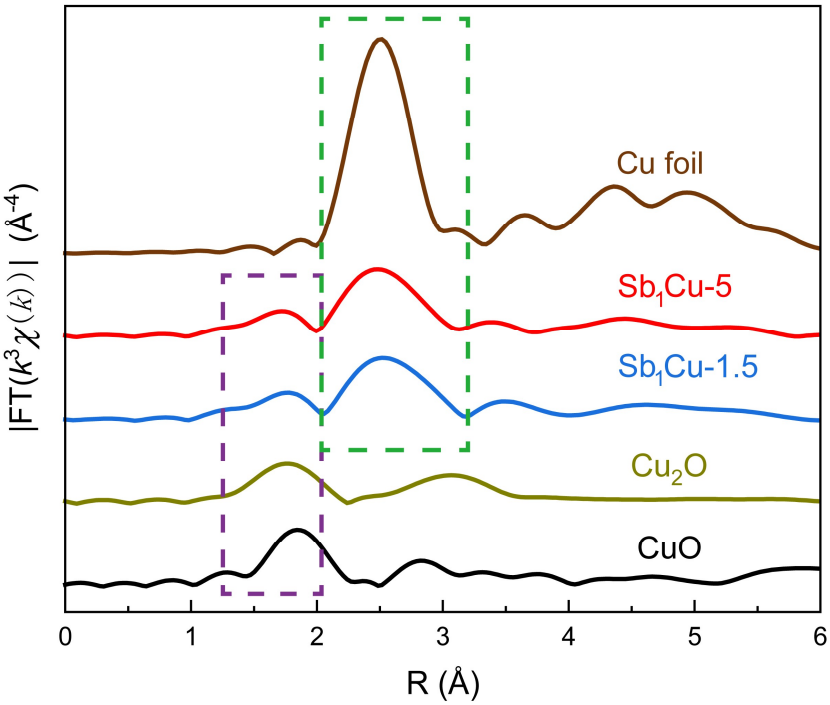


**Supplementary Fig. 8 | EXAFS spectra at the Cu *K*-edge of the as-prepared $Sb_1Cu$ catalysts.** Cu, CuO and $Cu_2O$ were used for references. The major peaks at approximately 2.50 Å were assigned to the Cu-Cu bond (highlighted in the green rectangle), while the Cu-O bond (peaks at approximately 1.75 Å, highlighted in the purple rectangle) was also observed due to partial oxidation in air, which was consistent with the XRD and XPS results.

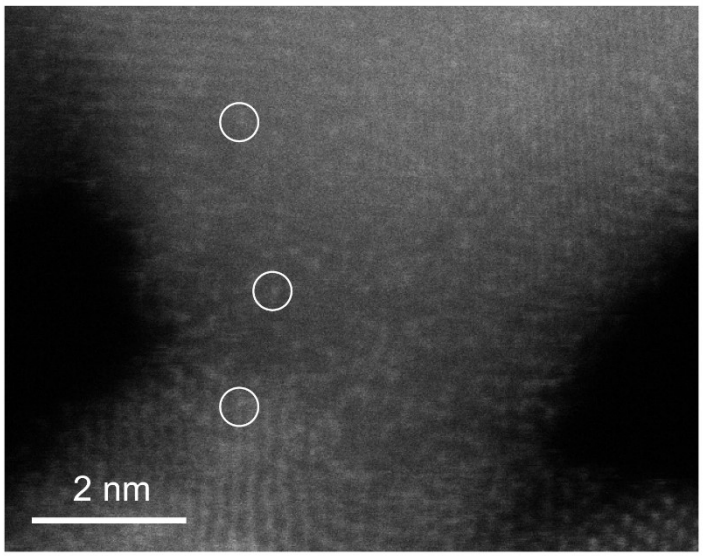


**Supplementary Fig. 9 | HAADF-STEM image of the as-prepared $Sb_1Cu$-1.5 catalyst.** White circles highlight isolated Sb atoms.

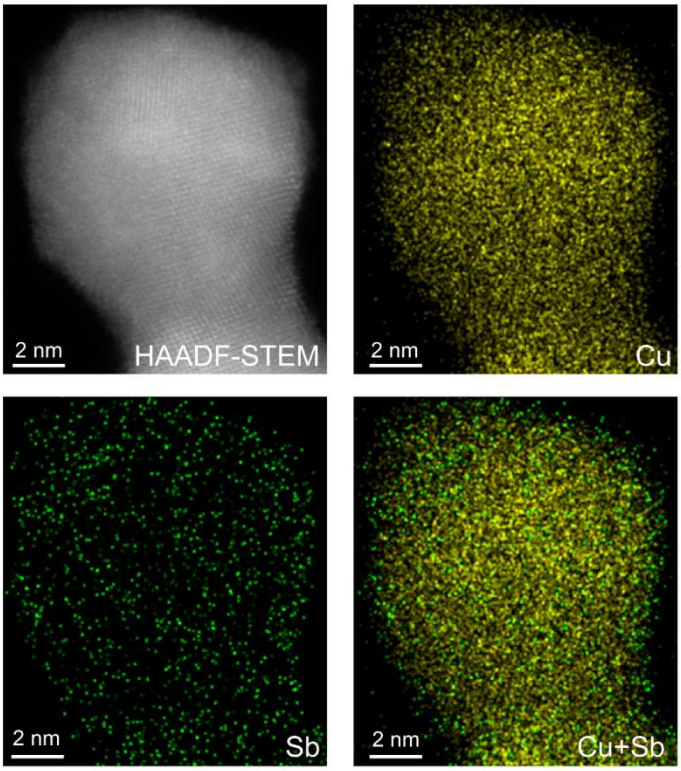


**Supplementary Fig. 10 | STEM-EDS mapping of the as-prepared $Sb_1Cu$-1.5 catalyst.** The image shows an even distribution of Sb in the Cu host.

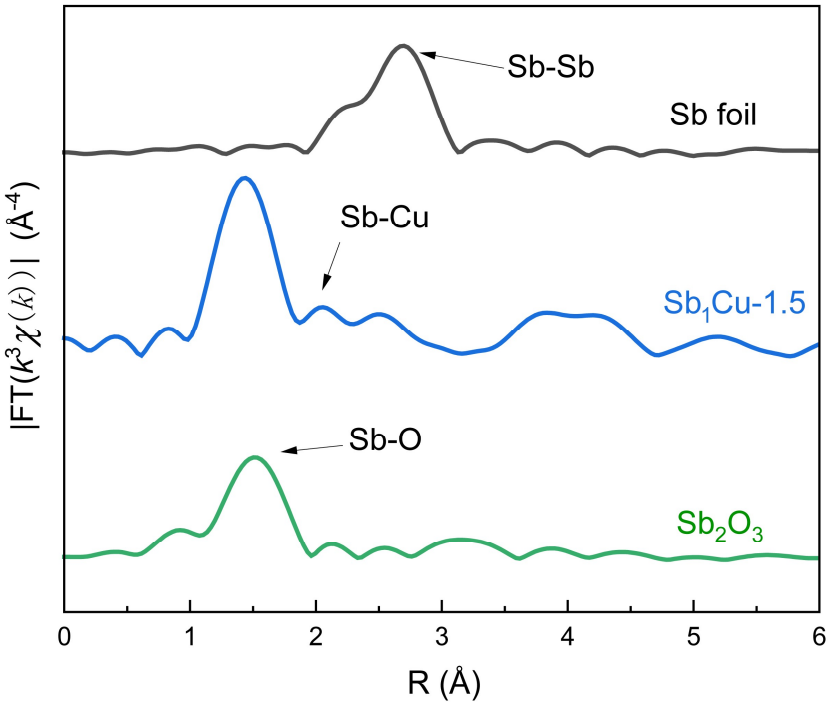


**Supplementary Fig. 11 | Sb *K*-edge EXAFS spectra of the as-prepared $Sb_1Cu$-1.5 catalyst without phase correction.** Sb foil and $Sb_2O_3$ are used as references. Peaks assigned to the Sb-Cu bond, together with the absence of the Sb-Sb bond, proved atomic Sb-Cu interfaces in the as-prepared $Sb_1Cu$-1.5 catalyst.

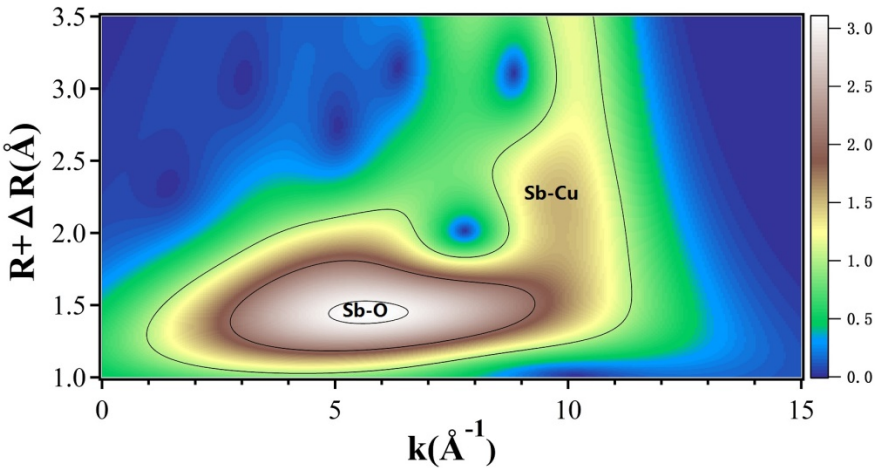


**Supplementary Fig. 12 | EXAFS WT for the $Sb_1Cu$-1.5 catalyst.** The Y-axis of the WT plots shows the radical distance, and the X-axis reflects the k-space resolution of the backscattering atom. Both the Sb-O bond and Sb-Cu bond can be clearly observed, verifying the formation of $Sb_1Cu$ interfaces.

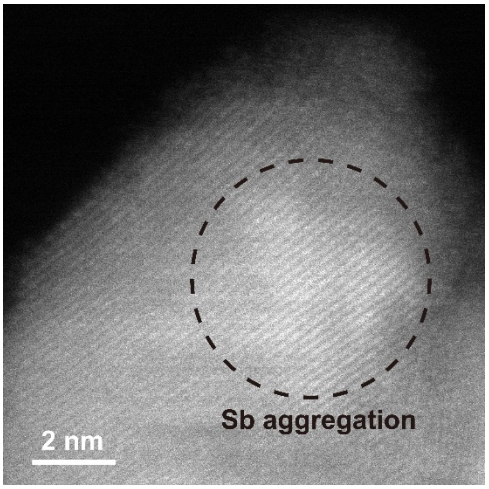


**Supplementary Fig. 13 | HAADF-STEM image of the $Sb_1Cu$-10 catalyst.** The black circle highlights Sb aggregation, confirming the formation of Sb clusters in the $Sb_1Cu$-10 catalyst.

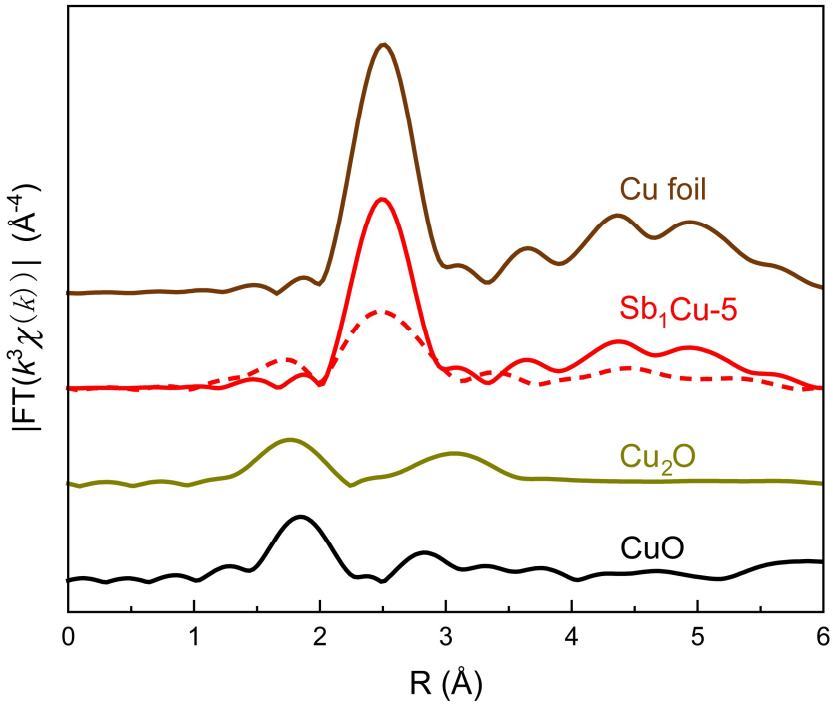


**Supplementary Fig. 14 | *In situ* Cu *K*-edge EXAFS spectra of the $Sb_1Cu$-5 catalyst under $CO_2RR$ conditions.** Spectra of $Sb_1Cu$-5 under OCP (dashed line) and -1.0 V *vs.* RHE (solid line) are shown in the figure, with Cu, $Cu_2O$ and CuO as references. The strengthened Cu-Cu peak (at approximately 2.50 Å) and disappearing Cu-O peak reconfirmed that metallic Cu was formed under the $CO_2RR$.

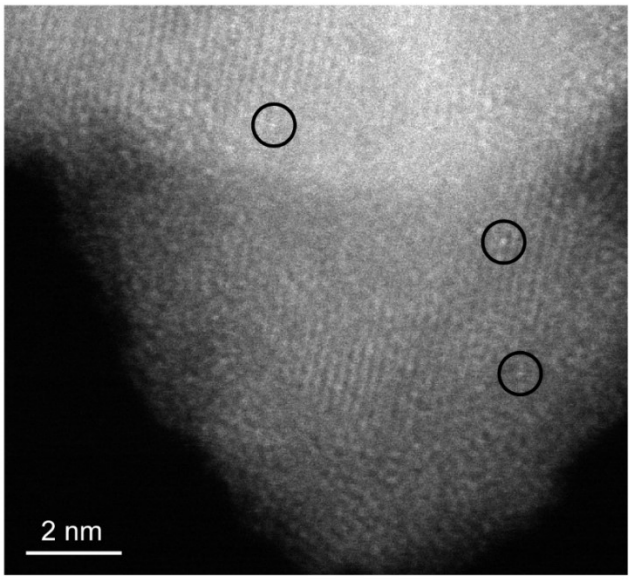


**Supplementary Fig. 15 | Post-catalysis HAADF-STEM images of the $Sb_1Cu$-5 catalyst.** The Sb single atoms were still mono-dispersed among the Cu matrix after $CO_2RR$, highlighted in black circles.

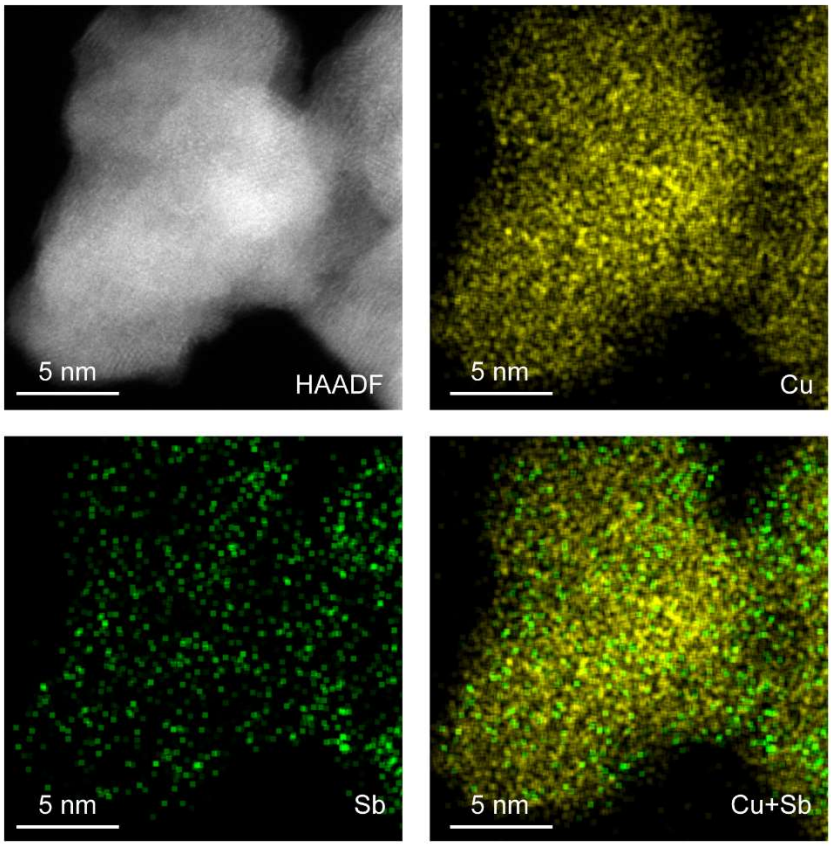


**Supplementary Fig. 16 | STEM-EDS mapping of the $Sb_1Cu$-5 catalyst after long-term electrolysis.** The homogeneous distribution of Sb in the Cu matrix was maintained after the $CO_2RR$.

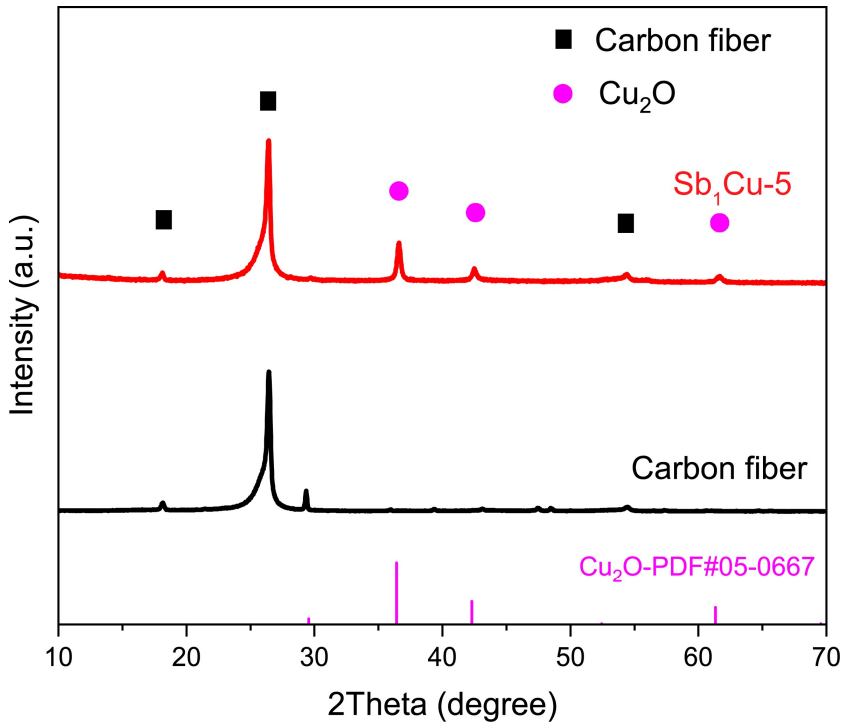


**Supplementary Fig. 17 | XRD pattern of post-catalysis $Sb_1Cu$-5 catalyst on the GDL.** The peaks of carbon fiber from the GDL were excluded, and the spectra were consistent with the $Cu_2O$ reference because of the rapid oxidization in air during *ex situ* XRD measurements.

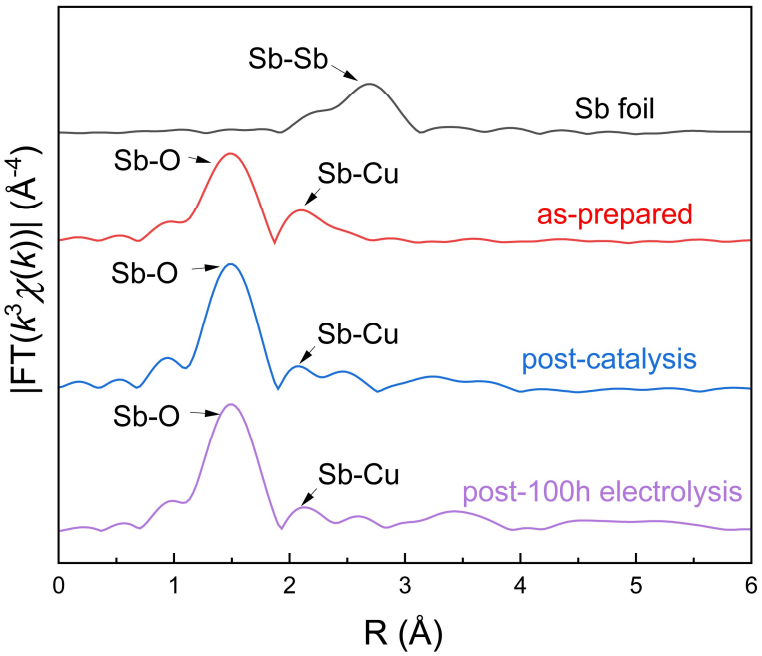


**Supplementary Fig. 18 | *Ex situ* Sb *K*-edge EXAFS spectra of the $Sb_1Cu$-5 catalyst after 100 h of continuous electrolysis without phase correction.** Sb foil is used as a reference. Peaks assigned to the Sb-Cu bond, together with the absence of the Sb-Sb bond, proved robust atomic Sb-Cu interfaces in the $Sb_1Cu$-5 catalyst after 100 hours of continuous electrolysis. In addition, the as-prepared sample and the sample after 30 min of electrolysis in the flow cell are also shown for comparison. The $Sb_1Cu$-5 catalyst after 100 hours of electrolysis in the H-cell showed almost the same Sb coordination structure as the as-prepared and post-catalysis samples, demonstrating the intrinsic long-term stability of the catalyst.

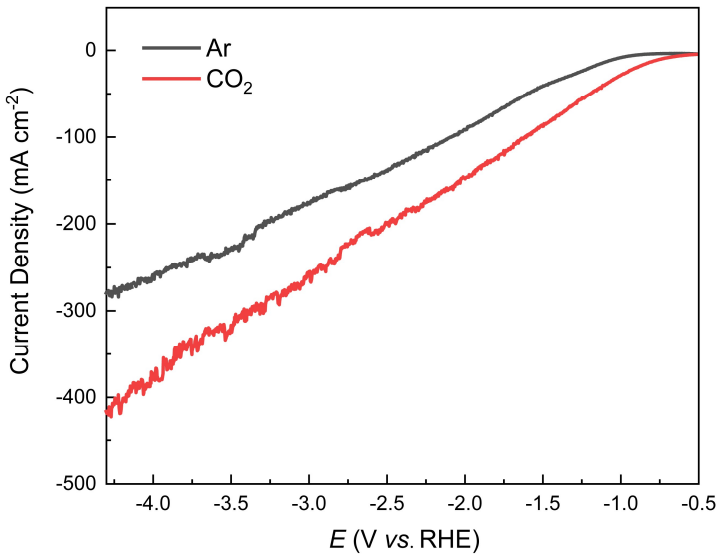


**Supplementary Fig. 19 | LSV of $Sb_1Cu$-5 catalyst.** The polarized curves were collected in a conventional three-electrode flow cell system using a scan rate of 0.1 V $s^{-1}$. 0.7 mL $min^{-1}$ 0.5 M $KHCO_3$ electrolyte and 30 sccm $CO_2$ or Ar flow were provided. The values of potential were presented without i-R compensation.

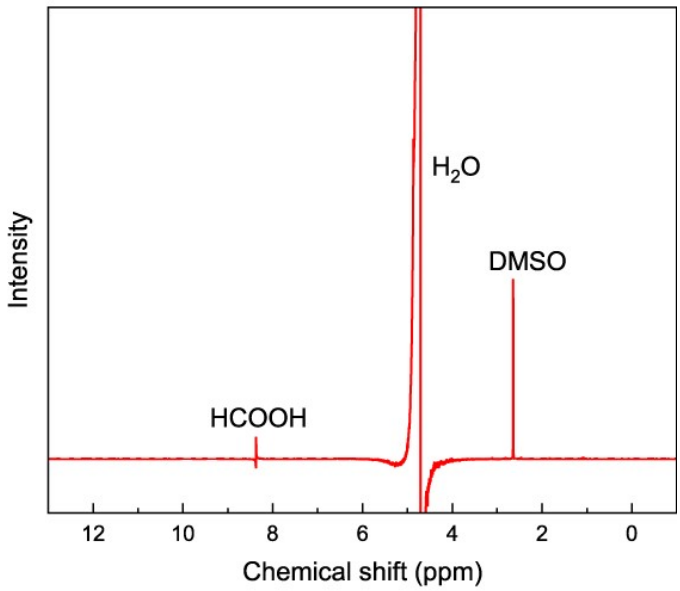


**Supplementary Fig. 20 | Typical $^{1}$H NMR spectrum of liquid product for $CO_2$RR on $Sb_1Cu$-5 catalyst.** No other peak except HCOOH and DMSO (internal standard) was observed, proving that HCOOH was the only liquid product on the $Sb_1Cu$-5 catalyst.

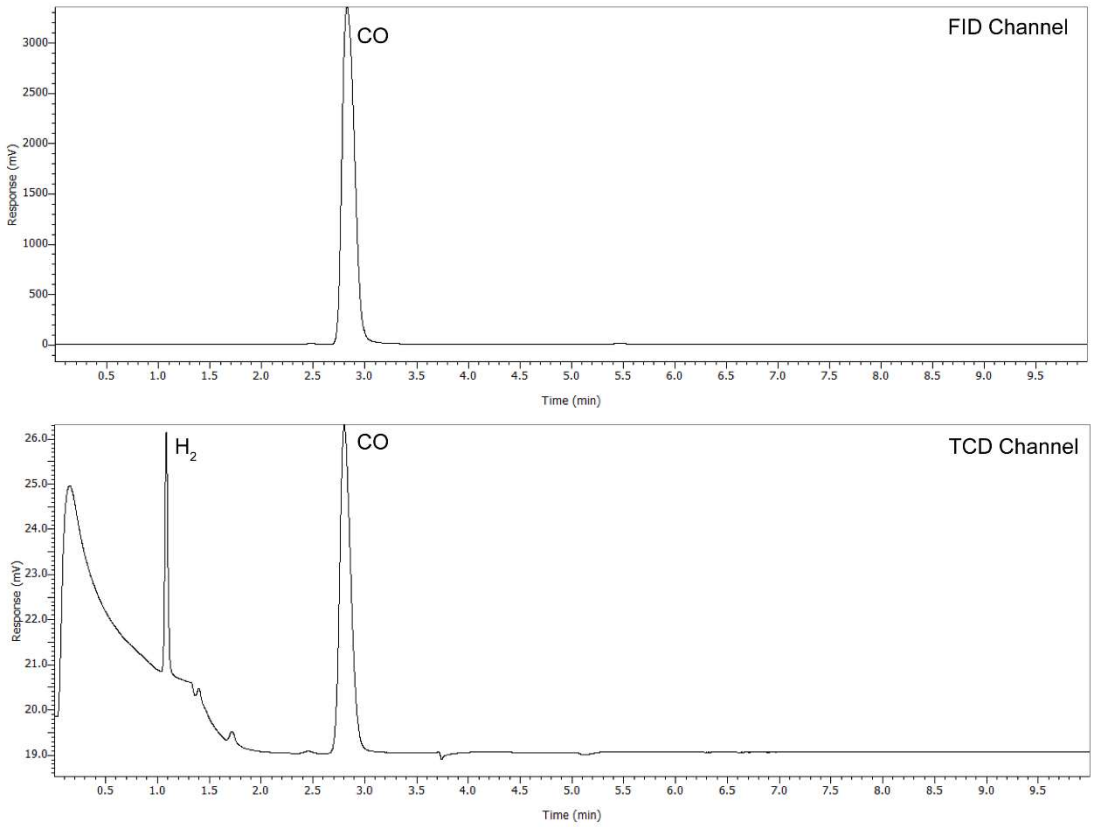


**Supplementary Fig. 21 | Typical GC response to gas products of the $CO_2$RR on the $Sb_1Cu$-5 catalyst.** The GC spectra verified $H_2$ and CO as the gas products, excluding $CH_4$ and $C_2H_4$ production.

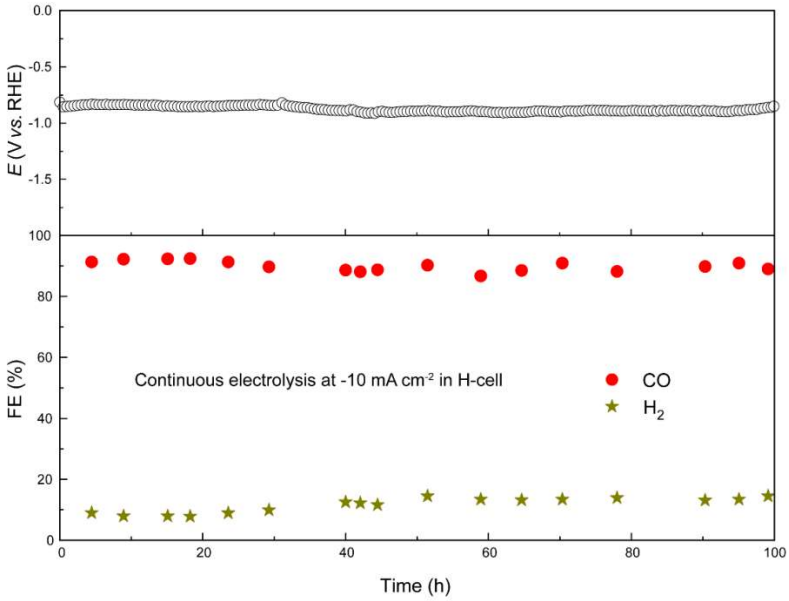


**Supplementary Fig. 22 | Stability test at a current density of -10 mA cm$^{-2}$ in an H-cell for 100 h.** To explore the intrinsic stability of $Sb_1Cu$-5 catalysts, we used an H-cell as the reaction reactor, which could avoid flooding and carbonation problems in MEA. The $FE_{CO}$ of approximately 90% during 100 h of continuous electrolysis and the stable cathode potential confirmed the impressive stability of the catalyst.

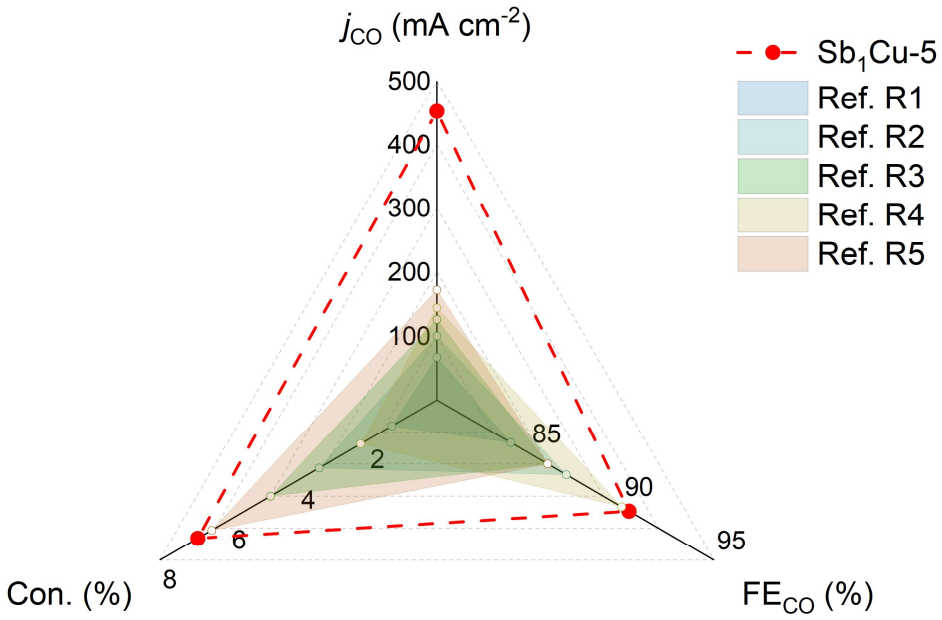


**Supplementary Fig. 23 | Comparison of the CO partial current density ($j_{CO}$), CO Faradaic efficiency ($FE_{CO}$) and conversion rate of $CO_2$-to-CO (Con.) with those of state-of-the-art CO-selective electrocatalysts.** [Ref. R1: *Angew. Chem. Int. Ed.* **61**, e202111683 (2022)]; [Ref. R2: *Nat. Commun.* **12**, 1449 (2021)]; [Ref. R3: *Angew. Chem. Int. Ed.* **60**, 11959-11965 (2021)]; [Ref. R4: *ACS Energy Lett.* **3**, 2835-2840 (2018)]; [Ref. R5: *Science* **365**, 367–369 (2019)]

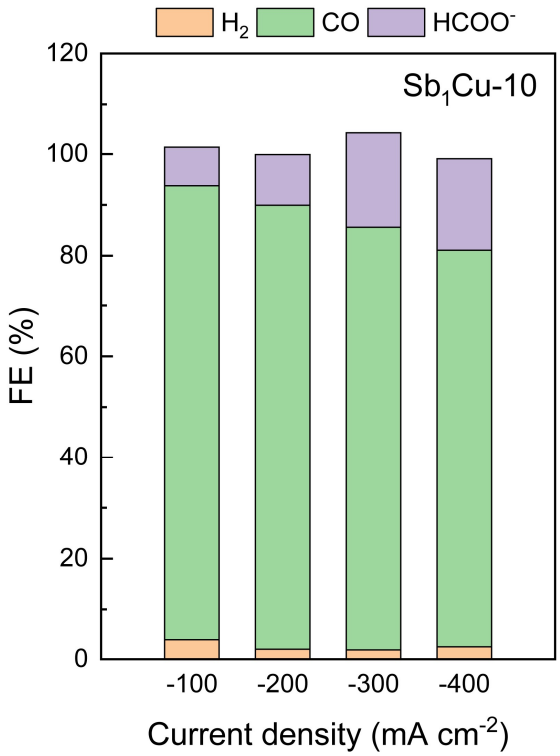


**Supplementary Fig. 24 | $CO_2$RR performance of the $Sb_1Cu$-10 catalyst in a flow cell.** As expected, due to the formation of Sb-Cu interfaces, negligible $C_{2+}$ formation and over 80% $FE_{CO}$ were found on $Sb_1Cu$-10, which confirmed the role of Sb-Cu interfaces in facilitating CO desorption and limiting C-C coupling. However, more formate produced on $Sb_1Cu$-10 compared with $Sb_1Cu$-5 was attributed to the formation of Sb clusters, considering that pure Sb exhibited relatively higher selectivity towards formate. This result manifested the importance of isolated Sb-Cu interfaces.

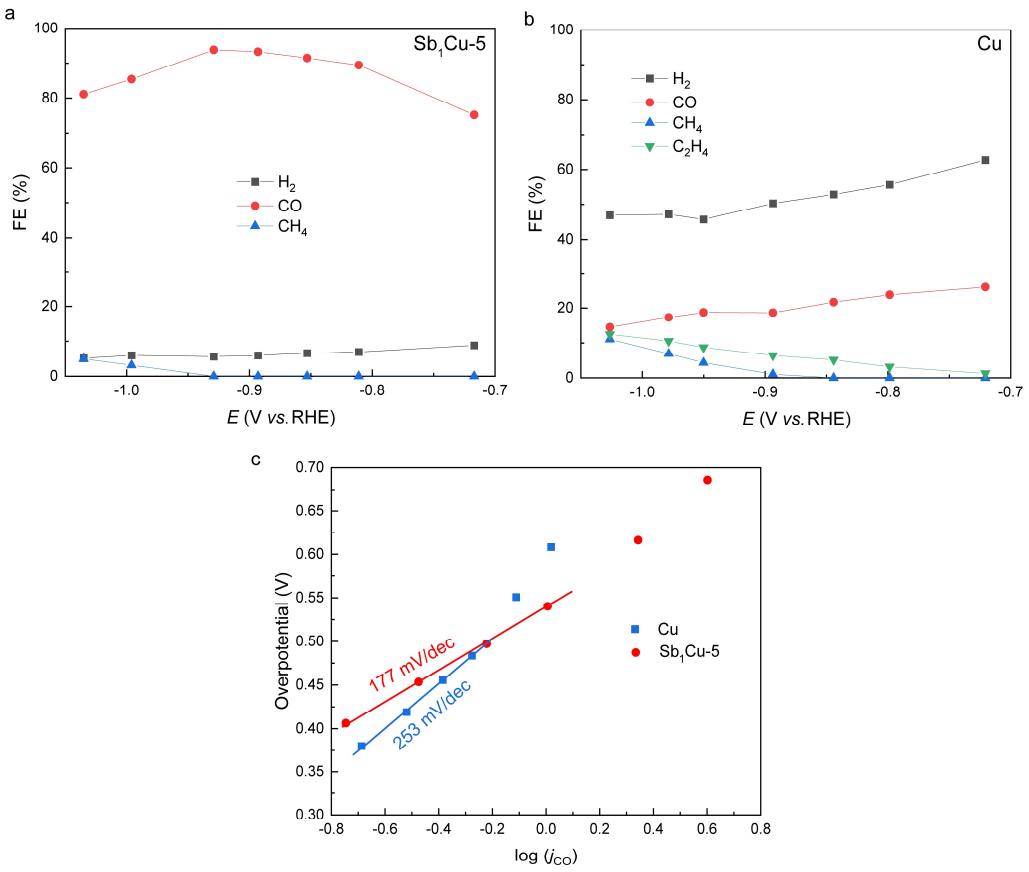


**Supplementary Fig. 25 | a, b) H-cell performance and c) Tafel plot of $Sb_1Cu$-5 and Cu catalysts.** In the H-cell, $FE_{CO}$ on $Sb_1Cu$-5 reached a maximum of 93.8% at -0.93 V and maintained >80% over a wide potential window (-0.8 ~ -1.15 V). In contrast, $FE_{CO}$ remained below 30% on Cu, and $C_2H_4$ production was observed, indicating C-C coupling. In the Tafel plot, the smaller slope of the $Sb_1Cu$-5 catalyst indicated faster kinetics towards the $CO_2RR$ to CO. Supplementary Table 5 shows the standard values of the Tafel slopes. A Tafel slope larger than 118 mV $dec^{-1}$ indicated the RDS of the first electron transfer $CO_2$-to-$*CO_2^-$. Deviation from the standard value was attributed to the asymmetry factor ($\alpha \neq 0.5$).

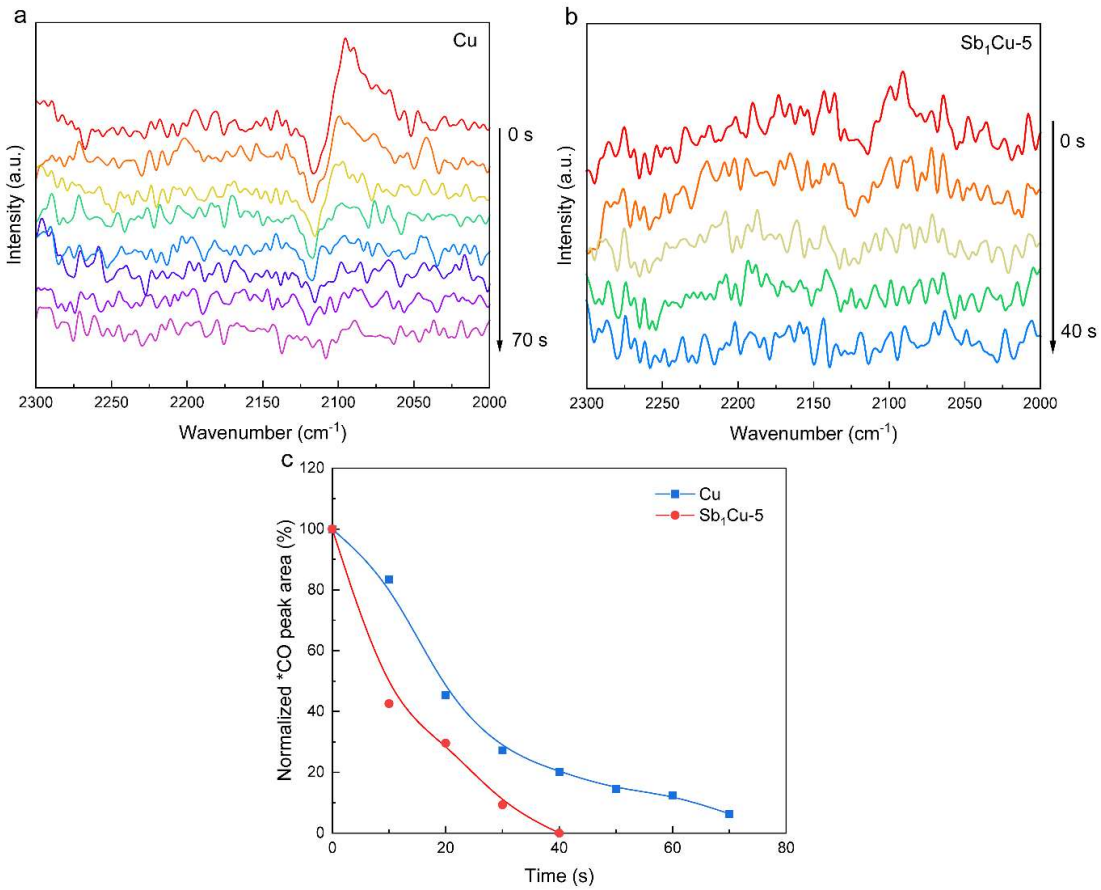


**Supplementary Fig. 26 | *In situ* ATR-SEIRAS spectra of a) Cu and b) $Sb_1Cu$-5 under an Ar sweep after suspension of the applied potential and c) attenuation of the *CO peak area with time.** To further confirm the better ability of CO desorption on $Sb_1Cu$-5, we investigated the *CO retention time under an Ar sweep. The faster attenuation rate and shorter retention time of *CO on $Sb_1Cu$-5 than Cu manifested its lower binding energy of *CO and better ability of CO desorption.

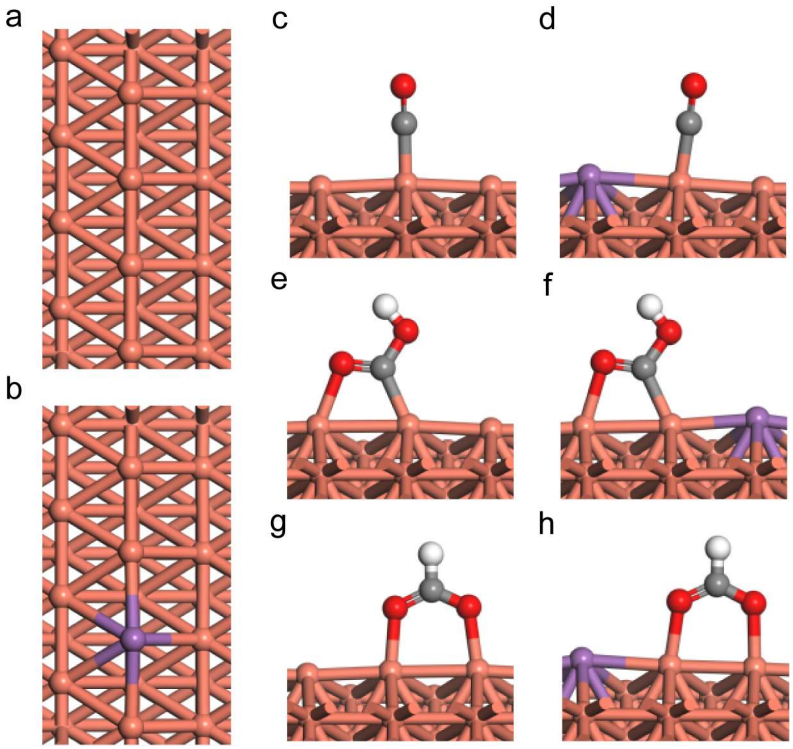


**Supplementary Fig. 27 | Surface structures.** Cu, Sb, C, O and H are represented in orange, purple, gray, red and white, respectively. The surface structures of a) Cu (211) and b) $Sb_1Cu$-5 (211). The adsorption states of CO* on c) Cu (211) and d) $Sb_1Cu$-5 (211). The adsorption states of COOH* on e) Cu (211) and f) $Sb_1Cu$-5 (211). The adsorption states of HCOO* on g) Cu (211) and h) $Sb_1Cu$-5 (211).

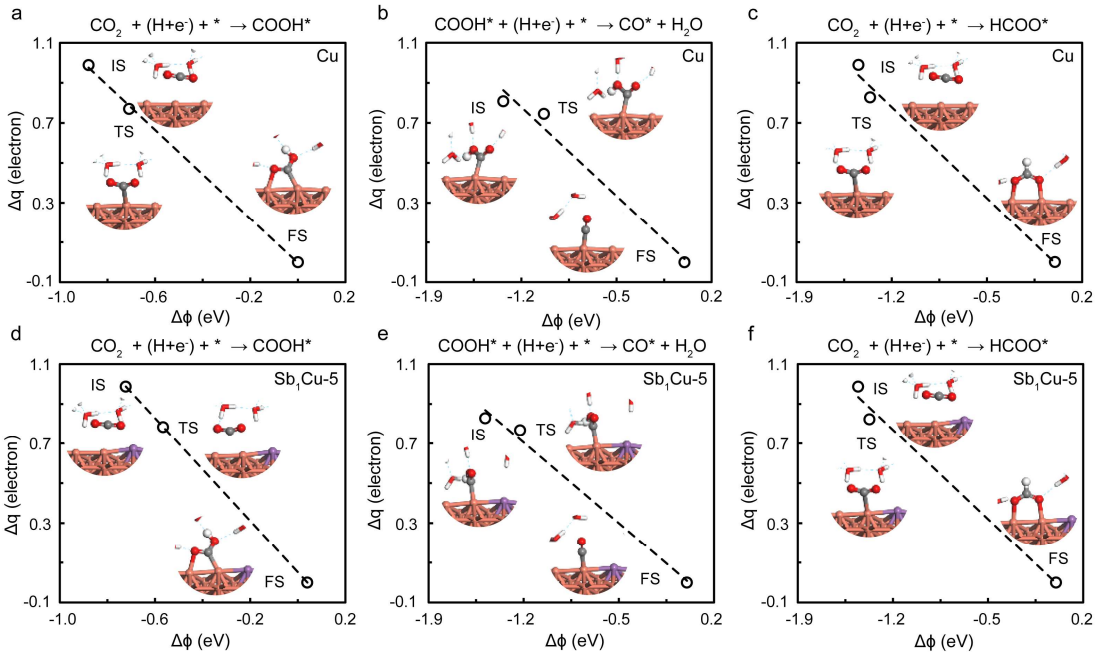


**Supplementary Fig. 28 | The scheme of 'charge-extrapolation'.** Linear relations between the amount of electrons transferred from the electrode to the water layer ($\Delta q$) and the relative work function of the system ($\Delta \Phi$) at the initial (IS), transition (TS) and final (FS) states for $CO_2$ protonation and CO* formation. Cu, Sb, C, O and H are represented in orange, purple, gray, red and white, respectively.

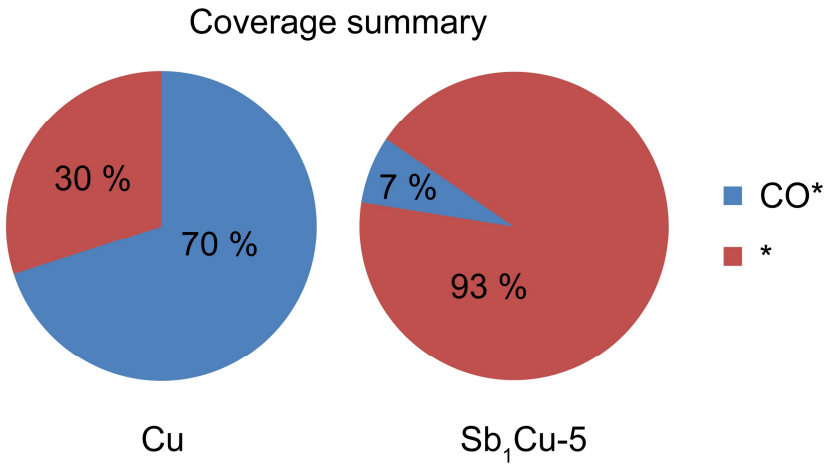


**Supplementary Fig. 29 | Coverage summary at the steady state for the $CO_2$RR on Cu (211) and $Sb_1$Cu-5 (211).** The CO* coverage takes up 70% of the total sites for the $CO_2$RR on pristine Cu, providing a much higher possibility for C-C coupling. In contrast, CO* occupies only 7% coverage on $Sb_1$Cu-5 (211). The results are consistent with *in situ* ATR-SEIRAS and *in situ* Raman measurements.

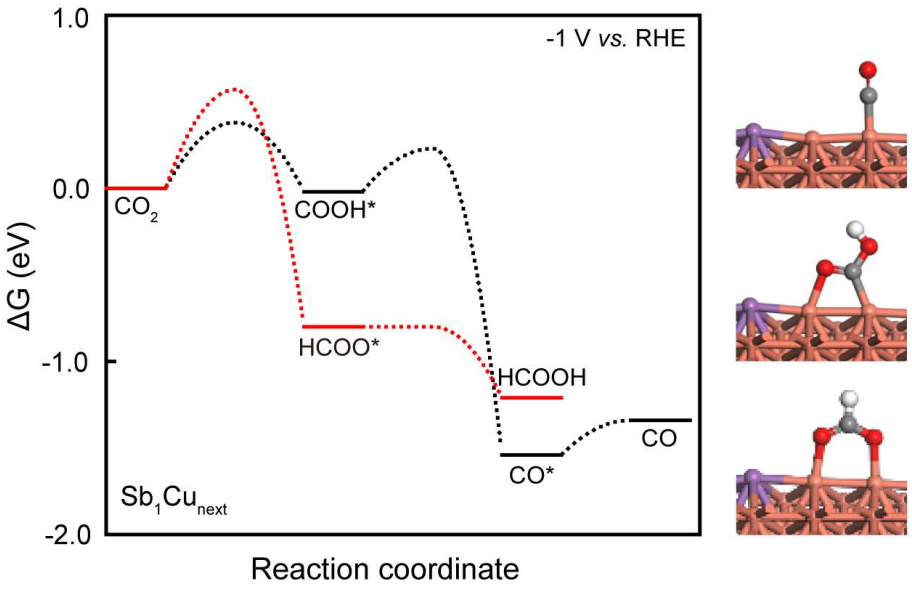


**Supplementary Fig. 30 | $CO_2$RR to CO and HCOOH on Cu site (next-nearest to Sb atom) on $Sb_1Cu$-5 (211).** The adsorption structures are shown on the right, where Cu, Sb, C, O and H are represented in orange, purple, gray, red and white, respectively.

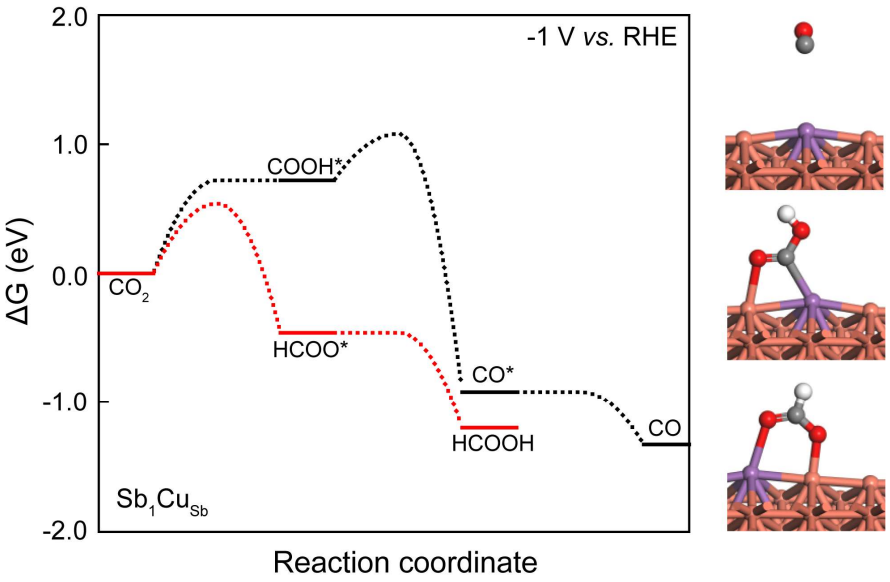


**Supplementary Fig. 31 | $CO_2$RR to CO and HCOOH on $Sb_1Cu\text{-}5(211)_{Sb}$.** The adsorption structures are shown on the right, where Cu, Sb, C, O and H are represented in orange, purple, gray, red and white, respectively. This revealed that the different concentrations of Sb may be the reason for the different products in different papers.

**Supplementary Table 1 | EXAFS fitting parameters at the Sb *K*-edge for $Sb_1Cu$ samples before and after the $CO_2RR$ ($S_0^2$=0.938).**

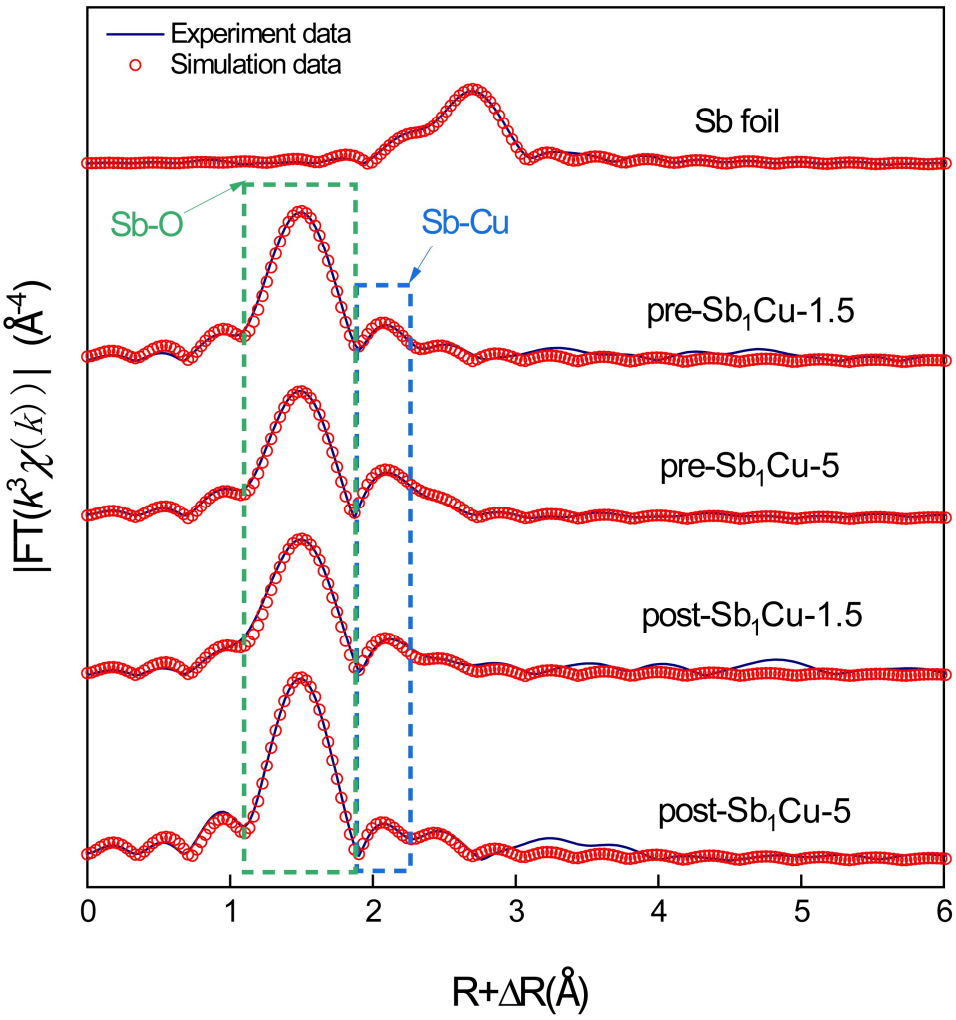


| Sample | Shell | $N^a$ | $R$(Å)$^b$ | $\sigma^2$(Å$^2$)$^c$ | $\Delta E_0$(eV)$^d$ | $R$ factor |
|---|---|---|---|---|---|---|
| Sb foil | Sb-Sb | 3 | 2.91 | 0.0039 | 8.3 | 0.0045 |
| pre-$Sb_1$Cu-1.5 | Sb-O | 5.4 | 1.98 | 0.0022 | 8.0 | 0.0015 |
| | Sb-Cu | 0.7 | 2.68 | 0.0071 | | |
| pre-$Sb_1$Cu-5 | Sb-O | 4.8 | 1.98 | 0.0029 | 7.9 | 0.0015 |
| | Sb-Cu | 2.4 | 2.64 | 0.0102 | | |
| post-$Sb_1$Cu-1.5 | Sb-O | 5.8 | 1.99 | 0.0037 | 8.3 | 0.0039 |
| | Sb-Cu | 0.9 | 2.68 | 0.0068 | | |
| post-$Sb_1$Cu-5 | Sb-O | 5.9 | 1.98 | 0.0018 | 9.9 | 0.0007 |
| | Sb-Cu | 1.0 | 2.58 | 0.0087 | | |

$^a N$: coordination numbers; $^b R$: bond distance; $^c \sigma^2$: Debye-Waller factors; $^d \Delta E_0$: inner potential correction. $R$ factor: goodness of fit. $S_0^2$ was set to 0.938 for Sb, according to the experimental EXAFS fit of the Sb foil reference by fixing CN as the known crystallographic value.

**Supplementary Table 2 | Performance of recently reported non-Cu-based $CO_2$-to-CO electrocatalysts in flow cells.**

| Catalyst | Potential (V *vs.* RHE) | $j_{CO}$ (mA $cm^{-2}$) | $FE_{CO}$ (%) | Ref. |
|---|---|---|---|---|
| **$Sb_1Cu$-5** | **-1.16** | **452** | **90.4** | **This work** |
| | **-1.13** | **360** | **90.0** | |
| Ni-SA/PCFM | -1.2 | 337 | 81 | *Nat. Commun.* **11**, 593 (2020) |
| $Fe^{3+}$-N-C | -0.45 | 94 | 94 | *Science* **164**, 1091-1094 (2019) |
| CoPc@Fe-N-C | -0.83 | 277 | 94 | *Adv. Mater.* **31**, 1903470 (2019) |
| Ni@NiNCM | -0.92 | 126 | 84 | *Angew. Chem. Int. Ed.* **60**, 11959-11965 (2021) |
| CoPc | / | 172 | 86 | *Science* **365**, 347-369 (2019) |
| Mg-$C_3N_4$ | -0.61 | 270 | 90 | *Angew. Chem. Int. Ed.* **60**, 25241-25245 (2021) |
| Zn/NC-NSs | -1.06 | 67 | 84 | *Angew. Chem. Int. Ed.* **61**, e202111683 (2022) |

**Supplementary Table 3 | Performance of recently reported Cu-based $CO_2$-to-CO electrocatalysts.**

| Catalyst | Potential (V *vs.* RHE) | $j_{CO}$ (mA $cm^{-2}$) | $FE_{CO}$ (%) | Ref. |
|---|---|---|---|---|
| **$Sb_1Cu$-5** | **-1.16** | **452** | **90.4** | **This work** |
| | **-1.13** | **360** | **90.0** | |
| $Cu/Ni(OH)_2$ | -0.5 | 3.7 | 92 | *Sci. Adv.* **3**, 9 (2017) |
| Cu-APC | -0.78 | 8.6 | 92 | *Nat. Chem.* **11**, 222-228 (2019) |
| $Cu\text{-}S_1N_3/Cu_x$ | -0.75 | 7.5 | 90 | *Angew. Chem. Int. Ed.* **60**, 24022–24027 (2021) |
| $V\text{-}CuInSe_2$ | -0.6 | 70 | 92 | *Adv. Mater.* **34**, 2106354 (2022) |
| $CuCo_{1.0}$ | / | 60.5 | 97.4 | *ACS Sustain. Chem. Eng.* **8**, 12561−12567 (2020) |
| CuZn NW | -1.0 | 14.4 | 90 | *ACS Catal.* **12**, 2741−2748 (2022) |
| $Cu_{97}Sn_3$ | -0.45 | 120 | 87 | *Nat. Commun.* **12**, 1449 (2021) |
| $Cu/Cu_2O\text{-}Sb\text{-}5$ | / | 110 | 91 | *J. Mater. Chem. A* **9**, 23234 (2021) |

**Supplementary Table 4 | Performance of recently reported Sb-Cu electrocatalysts in an H-cell.**

| **Catalyst** | **Potential (V *vs.* RHE)** | **$j_{CO}$ (mA $cm^{-2}$)** | **Mass activity (mA $mg^{-1}$)** | **$FE_{CO}$ (%)** | **Stability (h)** | **Ref.** |
|---|---|---|---|---|---|---|
| $Sb_1Cu$-5 | **-0.85** | **9.2** | **9.2** | **92.3** | **100** | **This work** |
| $Cu_2Sb$ NA/CF | -0.9 | 6 | - | 86.5 | 2 | *Nano Res.* **14**, 2831-2836 (2021) |
| $Sb_{0.22}Cu$ | -0.8 | 16.2 | 5.4 | 95 | 10 | *Appl. Catal. B: Environ.* **306**, 121089 (2022) |
| Sb-Cu | -1.1 | 4.7 | 2.9 | 80 | 12 | *ACS Catal.* **11**, 6846-6856 (2021) |

**Supplementary Table 5 | Tafel slope for different possible RDSs during the $CO_2$RR to CO.**

| Possible RDS | Type[a] | Tafel slope (mV $dec^{-1}$)[b] |
|---|---|---|
| $CO_2 + * + e^- \rightarrow *CO_2^-$ | ET | 118 |
| $*CO_2^- + H_2O \rightarrow *COOH + OH^-$ | PT | 59 |
| $*COOH + e^- \rightarrow *COOH^-$ | ET | 39 |
| $*COOH^- \rightarrow *CO + OH^-$ | PT | 30 |
| $*CO \rightarrow CO + *$ | D | 30 |
| [a]*ET* electron transfer, *PT* proton transfer, *D* desorption<br>[b]Assuming $\alpha = 0.5$ | | |

**Supplementary Table 6 | Elementary steps for FTacV simulations and key fitting parameters.**

| Type | Elementary steps | Fitting parameters |
|---|---|---|
| Electron transfer | $CO_2 + * + e^- \rightarrow *CO_2^-$ | $k_s = 6.5$ cm $s^{-1}$<br>$\alpha = 0.34$ |
| Chemical reaction | $*CO_2^- + H_2O \rightarrow *COOH + OH^-$ | $k_f = 2.5\times10^3$ $L\cdot mol^{-1}\cdot s^{-1}$<br>$k_b = 1.5$ $L\cdot mol^{-1}\cdot s^{-1}$ |
| Electron transfer | $*COOH + e^- \rightarrow *COOH^-$ | $k_s = 7$ cm $s^{-1}$<br>$\alpha = 0.37$ |
| Chemical reaction | $*COOH^- \rightarrow *CO + OH^-$ | $k_f = 2.0\times10^4$ $s^{-1}$<br>$k_b = 1.5$ $L\cdot mol^{-1}\cdot s^{-1}$ |
| $k_s$ standard rate constant, $\alpha$ transfer coefficient for electron transfer steps;<br>$k_f$ forward rate constant, $k_b$ backward rate constant for chemical reactions. | | |